Thermotropic liquid crystal enables efficient and stable perovskite solar modules

Yi Yang,[1†] Cheng Liu,[1†] Yong Ding,[2,3†] Bin Ding,[2†] Jian Xu,[4†] Ao Liu[1], Jiaqi Yu,[1] Luke Grater,[4] Huihui Zhu[1], Shreyash Sudhakar Hadke[5], Vinod K. Sangwan[5], Abdulaziz S. R. Bati,[1] Xiaobin Hu[5], Jiantao Li,[6] So Min Park,[1] Mark C. Hersam[1,5,7] Bin Chen,[1,4*] Mohammad Khaja Nazeeruddin,[2*] Mercouri G. Kanatzidis,[1*] Edward H. Sargent[1,4,7*]

[1]*Department of Chemistry, Northwestern University, 2145 Sheridan Rd, Evanston, Illinois 60208, United States*
[2]*Institute of Chemical Sciences and Engineering, Institute of Chemical Sciences and Engineering, EPFL, Lausanne, 1015, Switzerland*
[3]*State Key Laboratory of Alternate Electrical Power System with Renewable Energy Sources, North China Electric Power University, Beijing 102206, China.*
[4]*Department of Electrical and Computer Engineering, University of Toronto, 35 St George Street, Toronto, Ontario, M5S 1A4, Canada*
[5]*Department of Materials Science and Engineering, Northwestern University, 2220 Campus Dr, Evanston, Illinois 60208, United States*
[6]*Chemical Sciences and Engineering Division, Argonne National Laboratory, 9700 S Cass Ave, Lemont, Illinois 60439, United States*
[7]*Department of Electrical and Computer Engineering, Northwestern University, 2145 Sheridan Rd, Evanston, Illinois 60208, United States*

†These authors contributed equally to this work.

*E-mails: bin.chen@northwestern.edu (B.C.), mdkhaja.nazeeruddin@epfl.ch (M.K.N.), m-kanatzidis@northwestern.edu (M.G.K.), ted.sargent@northwestern.edu (E.H.S.)

Abstract

Perovskite solar cells (PSCs) have seen impressive progress in performance and stability; yet maintaining PCE when scaling area remains a challenge. Here we find that the additives used to passivate large-area perovskite films often co-precipitate with perovskite crystallization and aggregate at interfaces, and that these contribute to defects and to spatial inhomogeneity. We develop criteria for additives that can prevent their evaporative precipitation and enable uniform passivation in perovskite films. This leads us to explore families of liquid crystals for the combination of (1) melting point below the perovskite processing temperature (2) functionalization for perovskite passivation and (3) hydrophobicity to confer enhanced device stability. We find that thermotropic liquid crystals enable large-area perovskite films that are uniform, low in defects, and stable: we document as a result modules having a certified PCE of 21.6% at an aperture area of 31 cm^2. These retain performance under the damp-heat test (ISOS-D-3, 85% relative humidity, 85°C) with T_{86} of

1200 hours, and show high resistance to reverse bias with (ISOS-V-1, negative V_{mpp}) and without bypass diodes.

Main text

Perovskite solar cells (PSCs) have seen impressive progress,[1-4] including in methods of manufacture such as slot-die coating and vacuum quenching. Nevertheless, a gap exists in module efficiency compared to cell: the highest certified quasi-steady-state efficiency of perovskite modules exceeding 30 cm^2 has been so far limited to 19.5%.[5-7] Defects are known to play a significant role - this attributed to local perturbations in stoichiometry.[8,9]

Incorporating additives, such as Lewis acids and bases, into the precursor solution, has been seen to suppress defect formation.[10-13] In early studies herein, though, we found that these additives tend to unevenly aggregate in the perovskite film during the process of co-precipitation with perovskite as the solvent evaporates,[14-16] - a phenomenon that could cause inhomogeneity within the perovskite film, thereby challenging the scale-up process.[17] Specifically, photoluminescence (PL) mapping reveals a full 3x variance in local PL intensity when we use both additive-free, and previously-reported-additive, film processing (**Supplementary Fig. 1**).

Liquid crystal properties and interactions with perovskite

We explored therefore additives capable of preventing the evaporative precipitation or crystallization of additives. Thermotropic liquid crystals, which have tunability in this regard, are controlled and understood through molecular design. We screened a family of six liquid crystals (**Supplementary Text**, **Supplementary Table 1**, **Supplementary Figs. 2, 3**) based on melting point, solubility, and binding energy with defect sites on perovskite (**Fig. 1a**, **b**), noted one candidate - (3,4,5-trifluoro-4'-(trans-4-propylcyclohexyl)biphenyl (TFPCBP) - that showed particular promise with respect to PL map uniformity (**Supplementary Fig. 4**) and device performance (**Supplementary Fig. 5**).

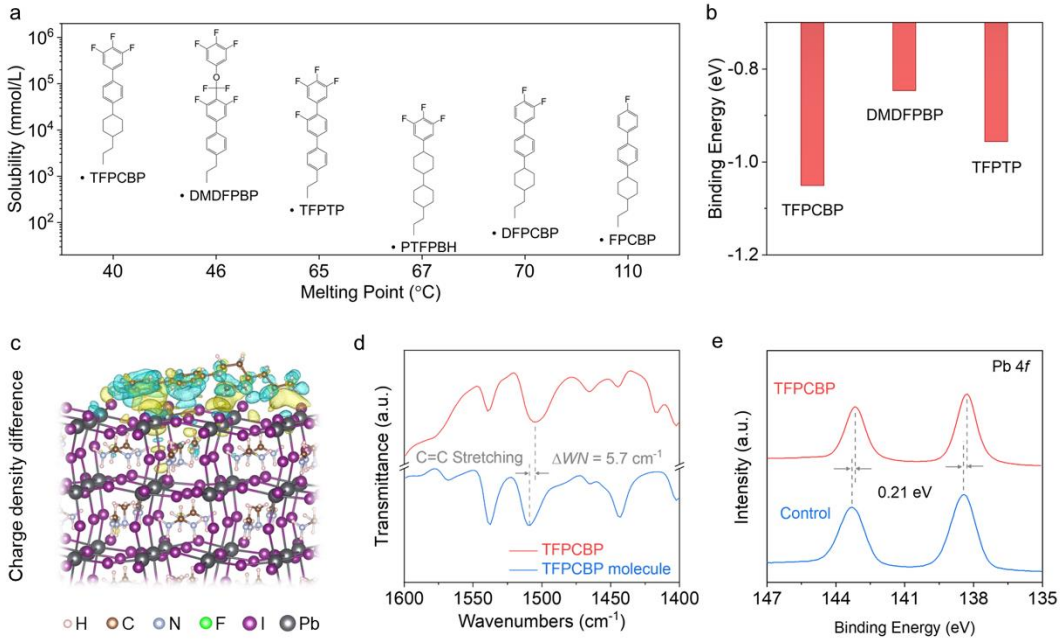

Fig. 1 | Characterization of liquid crystals and interactions with perovskite. a. Comparison of solubility and melting points of liquid crystal molecules. **b.** Binding energy of -$C_6H_2F_3$ group attached to the iodine vacancy defect. **c.** Charge density difference (blue, depletion; yellow, accumulation) of TFPCBP anchoring on the Pb-I terminated perovskite surface. **d.** FTIR of the TFPCBP-embedded perovskite film and the TFPCBP powder. **e.** XPS spectra of Pb 4*f* core levels.

We carried out density functional theory (DFT) calculations to study the interaction between TFPCBP and the perovskite. The neutral TFPCBP molecule has a dipole moment of 4.15 Debye (**Supplementary Fig. 6**) owing to the electron-withdrawing nature of the phenyl and F functional groups. Upon interacting with the formamidinium-I and Pb-I terminated perovskite surfaces, we found that TFPCBP exhibited a charge redistribution, particularly on the side (-$C_6H_2F_3$) characterized by the lowest electrostatic potential (**Fig. 1c** and **Supplementary Fig. 7**). Experimental analysis using Fourier transform infrared spectroscopy (FTIR) showed a frequency shift of 5 cm^{-1} at ~1500 cm^{-1} (**Fig. 1d**) corresponding to the carbon-carbon stretching vibrations in the aromatic ring,[18] and a shift of ~2 cm^{-1} at 1040 cm^{-1}, related to the carbon-fluorine stretching vibrations (**Supplementary Fig. 8**).[19] High-resolution X-ray photoelectron spectroscopy (XPS) analysis provided additional evidence of molecular interactions between TFPCBP and perovskite. The core level spectra of Pb 4*f* in perovskite and F 1*s* in TFPCBP exhibited a shift towards lower and higher binding energies, respectively, when TFPCBP was incorporated into the perovskite film (**Fig. 1e** and **Supplementary Fig. 9**).

Homogeneity and optoelectronic properties

Scanning electron microscopy (SEM) images (**Fig. 2a**) showed that the perovskite film with TFPCBP had crystal grains of ~ 2x the linear dimensions of controls, attributed to the slower crystal growth as observed from in-situ microscopy images (**Supplementary Fig. 10**). This was consistent with enhanced crystallinity and a tightened full width at half maximum (FWHM) seen in XRD (**Fig. 2b**). The crystal orientation was not affected by TFPCBP as shown in grazing incidence wide-angle *X*-ray scattering (GIWAXS) image (**Supplementary Fig. 11**). The control film showed the diffraction of δ-phase $FAPbI_3$ at $q_z = 0.88$ Å^{-1}, which was caused by perovskite degradation during ex-situ measurement exposed to humid air. However, the lack of δ phase for the TFPCBP film indicated increased environmental stability due to the hydrophobicity of TFPCBP (**Supplementary Fig. 12**). The time-of-flight secondary ion mass spectrometry (ToF-SIMS) demonstrated that the TFPCBP molecule was uniformly distributed throughout the entire film without accumulation at the interface/surface (**Fig. 2c**).

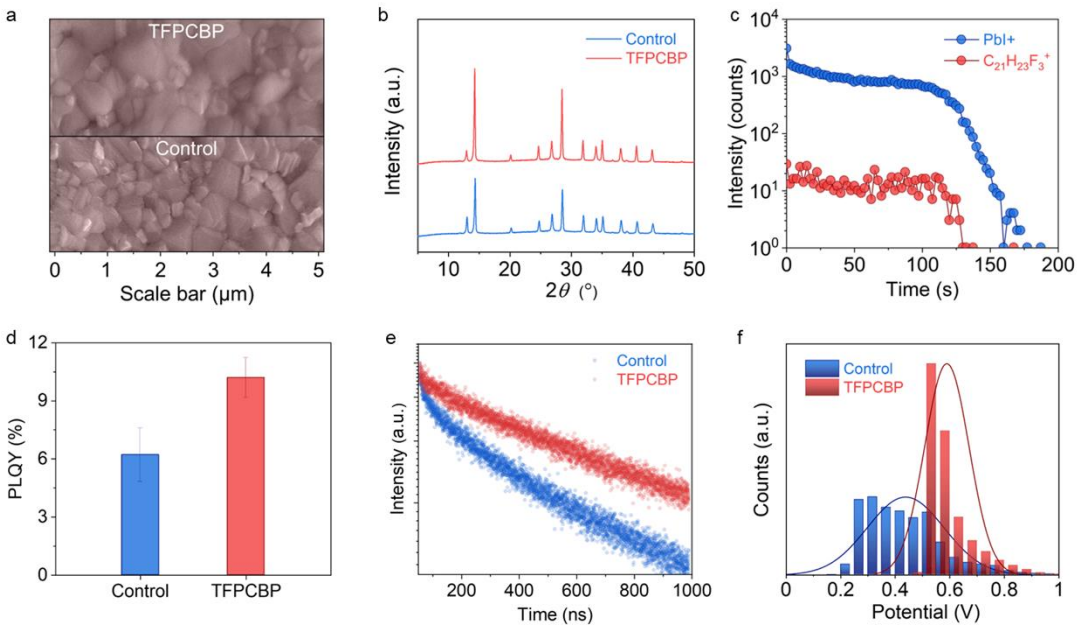

Fig. 2 | Characterization of perovskite films. a. SEM images of the control and TFPCBP-embedded perovskite films. **b.** XRD patterns of the perovskite films. **c.** SIMS depth profile of $C_{21}H_{23}F_3^+$ for the perovskite film with TFPCBP. **d.** PLQY of the fabricated perovskite films. **e.** TRPL spectra of perovskite films on glass substrates. **f.** KPFM potential distribution of perovskite films.

The final state of TFPCBP in the perovskite film was then investigated. Interestingly, we observed an amorphous feature of TFPCBP distributed at the grain boundaries from transmission electron microscopy (TEM) (**Supplementary Fig. 13**). This aligns with the absence of the TFPCBP peak in the XRD pattern of the TFPCBP-embedded perovskite film (**Fig. 2b** and **Supplementary**

Fig. 14). This could be attributed to: 1) the low melting point of TFPCBP, facilitating strong molecular diffusion during the perovskite crystallization, resulting in a uniform distribution along the narrow grain boundaries (**Supplementary Fig. 15**), and 2) the relatively large TFPCBP molecules, which hinders the aggregated crystallization of TFPCBP due to space confinement effect. This uniform distribution of additives without aggregation would result in uniform passivation effect on perovskite.

Also using DFT we looked at how TFPCBP adsorption affects defect formation in perovskite films. We considered the most common iodine vacancy defect.[20] We simulated two adsorption modes of TFPCBP (**Supplementary Fig. 16**) and found that the binding energy of the $-C_6H_2F_3$ group attached to the defect site (-1.05 eV) was higher than that of the alkyl chain group attached to the defect site (-0.47 eV), pointing to $-C_6H_2F_3$ as the most active functional group in TFPCBP from the point of view of interaction with the perovskite surface. Notably, the introduction of TFPCBP led to an increase in the iodine vacancy formation energy from 1.18 eV to 1.27 eV, indicating its capacity to suppress defects. Consistent with this, the average photoluminescence quantum yield (PLQY) of the perovskite film was increased, as was the excited state lifetime (890 ns vs. 520 ns) following incorporation of TFPCBP (**Fig. 2 d, e**). Additionally, a decreased trap density of states was observed in the space charge limited current (SCLC) model (**Supplementary Fig. 17**).

PL maps show that the TFPCBP-embedded film has enhanced PL emission and narrower emission distribution (**Supplementary Fig. 18**), indicating improved film homogeneity and suppressed defect sites. Unintended defects can cause strong potential fluctuations, as shown in the Kelvin probe force microscopy (KPFM) potential distribution (**Fig. 2f**). The contact potential difference (CPD) is a critical parameter in the performance of electronic devices, especially in thin film devices, because it affects the energy level alignment at the interface and hence, the efficiency of charge transfer and transport across the interface. The CPD can also influence the optical properties of the thin films by altering the bandgap of the materials at the interface and thereby affecting the absorption and emission of light. By effectively implementing TFPCBP, the root-mean-square deviation of CPD was significantly reduced from 104 mV to 81 mV. This reduction indicates a decrease in potential variation, resulting in a more uniform perovskite film. The higher average CPD is expected to enhance the transport of holes across the interface between the perovskite layer and the hole transport layer.[21]

Photovoltaic performance

We fabricated solar cells in an n-i-p configuration, employing fluorine-doped tin oxide (FTO)/SnO_2/perovskite/2,2′,7,7′-tetrakis(N,Ndipmethoxyphenylamine)-9,9′-spirobifluorene (spiro-OMeTAD)/Au (**Fig. 3a**). The photovoltaic performance of these devices was evaluated with control and TFPCBP-embedded perovskite films. Control devices had PCEs of 23.5 +/- 0.6% while the TFPCBP had PCEs of 25.1 +/- 0.3% (**Supplementary Fig. 19**). The best TFPCBP device showed a PCE of 25.6%, with negligible hysteresis (**Fig. 3b**) and a stabilized power output (SPO) of 25.1% (**Fig. 3c**), compared to 24.4% for the champion control device (**Supplementary Fig. 20**). The J_{SC} obtained from the *J-V* characteristics was found to be consistent with the value integrated from the external quantum efficiency (EQE) spectrum, with a relative difference of less than 4%. (**Supplementary Fig. 21**).

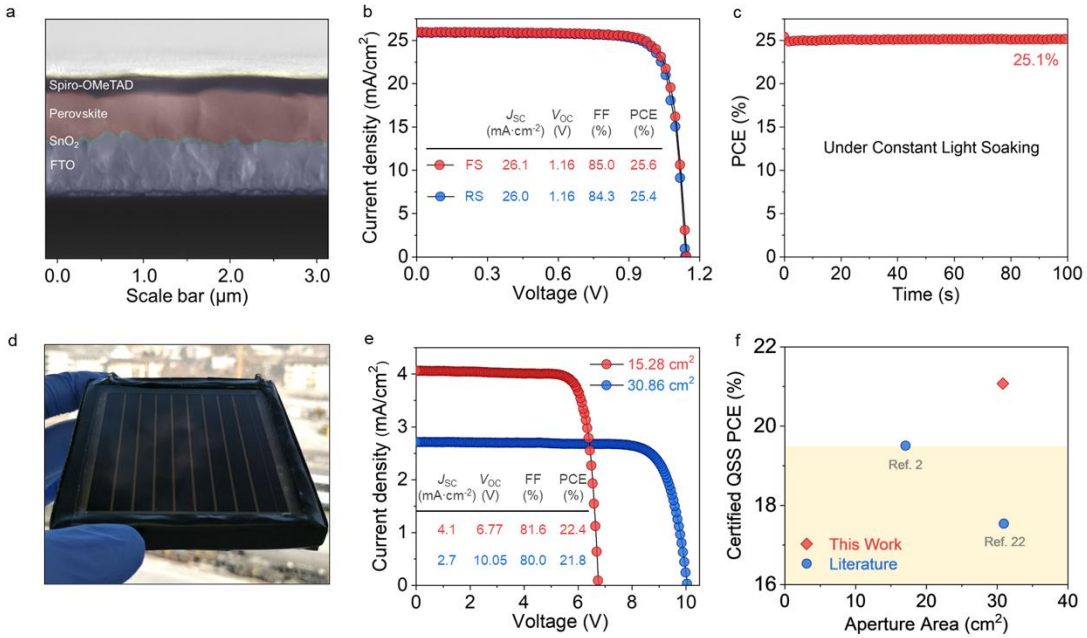

Fig. 3 | Photovoltaic performance of PSCs and perovskite solar modules. a. Cross-section SEM image of the fabricated PSC. **b.** *J-V* characteristics of the best-performing device. **c.** SPO of the best device. **d.** Photograph of the nine-subcell perovskite solar module. **e.** *J-V* characteristics of two perovskite minimodules with aperture areas of 15.28 and 30.86 cm^2, respectively. **f.** Statistics of certified QSS PCEs of n-i-p perovskite solar modules reported in the literature.

In order to investigate the impact of improved film homogeneity on large-scale applications, we fabricated perovskite solar modules using TFPCBP-embedded perovskite films (**Fig. 3d**). A module consisting of six subcells with an aperture area of 15 cm^2 exhibited a high PCE of 22.4%

(corresponding to an active-area PCE of 24.1%) with a V_{OC} of 6.77 V, a J_{SC} of 4.1 mA/cm^2, and an FF of 81.6% (**Fig. 3e**). When the aperture area is doubled, the module consisting of nine subcells with an aperture area of 31 cm^2 showed a PCE of 21.8% (corresponding to an active-area PCE of 24.0%) with a V_{OC} of 10.05 V, a J_{SC} of 2.7 mA/cm^2, and an FF of 80.0%. We sent the large module to the accredited National PV Industry Measurement and Testing Center (NPVM) in China for certification, and obtained a PCE of 21.6% (quasi-steady-state (QSS) efficiency of 21.1%) with a V_{OC} of 10.03 V, a J_{SC} of 2.7 mA/cm^2, and an FF of 79.7% (**Supplementary Fig. 22**). These modules possess, to the best of our knowledge, the highest certified PCE value reported among n-i-p perovskite solar modules (**Fig. 3f** and **Supplementary Table 2**).[2,22]

Stability study

To examine the stability of the perovskite films with and without TFPCBP, we evaluated the degree of degradation by subjecting the films to 85% relative humidity (RH) at 85°C. The crystallographic properties of the fresh and aged films were analyzed and compared (**Supplementary Fig. 23**). TFPCBP-embedded perovskite film exhibited higher resistance to damp heat, as evidenced by the decreased PbI_2/perovskite peak ratio (0.39) compared to that of the control film (0.85). Additionally, the PL mapping revealed that the control film suffered from a loss of photoactive phase after aging, while the TFPCBP-embedded perovskite film demonstrated a superior ability to maintain its original phase under external stresses (**Supplementary Fig. 24**). Therefore, we posited that the TFPCBP-based devices had improved stability.

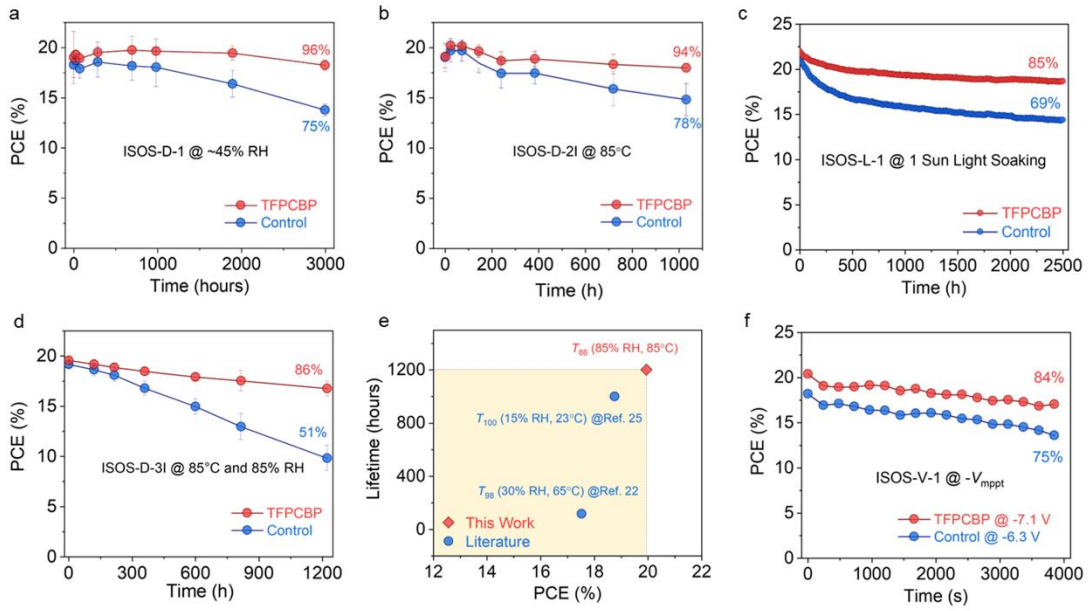

Fig. 4 | Stability of PSCs and perovskite solar modules. a. Humidity stability of small-sized PSCs under ~45% RH. **b.** Thermal stability of small-sized PSCs under constant heating at 85°C in N_2. **c.** Continuous MPP tracking of the unencapsulated small-sized PSCs under 1-sun illumination with N_2 flow. **d.** Stability of the encapsulated perovskite modules stored under ~85% RH and heating at 85°C. **e.** Statistics of the combination of certified PCEs and damp-heat stability of n-i-p perovskite solar modules reported in the literature. **f.** The reverse bias stability of perovskite modules (8 subcells) biasing at the -V_{mpp}, simulating the condition with the bypass diode. The error bars in the stability tests represent the standard deviation of PCEs.

To assess the impact of TFPCBP on device stability, we substituted the doped spiro-OMeTAD with poly[bis(4-phenyl)(2,4,6-trimethylphenyl)amine] to eliminate this HTL as a source of instability.[23] We tracked performance of unencapsulated solar cells under a ~45% RH ambient according to ISOS-D-1.[24] Following 3,000 hours of aging, the cells had low 4% (relative) PCE loss for the TFPCBP-based device, compared to 25% (relative) efficiency loss seen in the control devices (**Fig. 4a**). We then tested the solar cells under prolonged heat exposure at 85°C in nitrogen, applying the ISOS-D-2 procedure. TFPCBP-based devices maintained 94% of their initial PCE after 1,000 hours of continuous heating, while the control devices retained 78% of initial performance (**Fig. 4b**). The thermal cycling tests revealed no efficiency decline in the TFPCBP-based device after 90 cycles between -20˚C and 65˚C, suggesting the TFPCBP molecule has no discernible impact on device thermal cycle stability (**Supplementary Fig. 25**). Operating stability was investigated under 1-sun illumination (ISOS-L-1). The TFPCBP device maintained 85% of the initial PCE after maximum power point (MPP) operation over 2,500 h (**Fig. 4c**), compared to control device with 69% PCE retention.

We then evaluated the damp-heat stability of encapsulated modules using the ISOS-D-3 procedure, subjecting them to 85% RH at 85°C. The TFPCBP-based modules maintain 86% of initial efficiency after 1,200 hours, compared to 51% retention for the control (**Fig. 4d**). This represents the longest-lived damp-heat stability in literature among n-i-p perovskite solar modules (**Fig. 4e** and **Supplementary Table 2**).[22,25] In addition to damp-heat stability, reverse bias stability is critical for solar modules as it mimics the scenario of partially shaded modules caused by clouds, dirt, and trees, where shaded sub-cells are compelled to operate under reverse bias to match the current flow through the rest of the module.[26,27] To investigate this, we simulated both conditions without and with bypass diodes, i.e. shading one of the subcells and applying a constant -V_{mpp} (ISOS-V-1) in the dark. The shading tests were performed by entirely masking one of the subcells

under 1-sun illumination. As shown in **Supplementary Fig. 26a**, the target module exhibits a higher breakdown voltage of -11.68 V over -10.54 V for the control module and could recover 90% of its original efficiency compared to 80% for the control module after the shading test (**Supplementary Fig. 26b**). **Fig. 4f** presents the performance of modules in the context of constant reverse bias stress. The target module subjected to a negative bias of $-V_{mpp}$ = -7.13 V exhibits superior reverse-bias resilience, with 84% of the initial efficiency being retained over 1 hour. This compares to the control module that retained 75% efficiency at $-V_{mpp}$ = -6.31 V.

Conclusion

In this study, we propose a liquid crystal additive approach to realize homogeneous dispersion of additives and uniform passivation effect on perovskite grains, leveraging the phase behavior and functionalization properties offered by thermotropic liquid crystals. We find that TFPCBP leads to the best results comparing with six liquid crystals, both in film uniformity and in photovoltaic performance. The TFPCBP demonstrates uniform distribution along the grain boundaries in the amorphous form, owing to its high molecular diffusion capability during the perovskite crystallization process. The combined theoretical and experimental results indicate defect passivation from the electron-rich $-C_6H_2F_3$ group. This enables small-area PSCs with PCEs reaching 25.6% and perovskite modules with an aperture area of 31 cm^2 having a certified efficiency of 21.6% along with a long-term environmental stability.

Methods

Materials. $SnCl_2 \cdot 2H_2O$ (99.99%), urea (99%), HCl acid (37 wt. % in water), thioglycolic acid (TGA, 98%), CsI (99.99%), 4-tert-Butylpyridine (98%), and bis(trifluoromethanesulfonyl)-imide lithium salt (LiTFSI, 99.0%) were purchased from Sigma-Aldrich. PbI_2 (99.99%) and TFPCBP (98%) were purchased from TCI America™. Formamidinium iodide (FAI), methylammonium chloride (MACl), methylammonium iodide (MAI), phenylethylammonium iodide (PEAI), and FK209 Co(III) TFSI salt were purchased from Greatcell Solar Materials. All the materials were used as received without purification. N, N-dimethylformamide (DMF, 99.8%), dimethyl sulfoxide (DMSO, 99.7%), isopropanol (99.8%), acetonitrile (99.9%), and chlorobenzene (99.8%) were purchased from the Acros Organics. Spiro-OMeTAD and poly[bis(4-phenyl)(2,4,6-

trimethylphenyl)amine] were from the Xi'an polymer light technology corp.

Solar cell fabrication.

The electron transport layer (ETL) was deposited on the precleaned FTO substrates by the chemical bath deposition (CBD) method. The CBD solution was prepared by mixing 1.25 g of urea, 1.25 mL of HCl, 25 μL of TGA, and 275 mg of $SnCl_2 \cdot 2H_2O$ in 100 mL of deionized water. The substrates were put into a staining dish immersed in the above solution in an oven at 90°C for 5 hours. After cooling down to room temperature, the substrates were taken out for washing with isopropanol and then annealing at 190°C for 1 hour. Before perovskite deposition, the FTO/SnO_2 substrates were treated with UV ozone. The perovskite solution was prepared by adding 1.60 M PbI_2, 1.37 M FAI, 0.52 M MACl, 0.08 M MAI, and 0.07 M CsI to mixed DMF and DMSO solution with a volume ratio of 4:1. 4 mol% liquid crystals were added to the perovskite precursor as an additive. The perovskite films were deposited at 1000 rpm for 10 s and 5000 rpm for 30 s, respectively. At the 20 s during the second step, 150 uL chlorobenzene was dropped on the spinning films to facilitate perovskite nucleation and crystallization. The films were then annealed at 100 °C for 50 min and 150 °C for 10 min. 20 mM PEAI solution in isopropanol was spin-coated on the perovskite films at 5000 rpm for 20s. For the hole transport layer (HTL), 0.06 M spiro-OMeTAD was dissolved in chlorobenzene with additives of 0.2 M 4-tert-Butylpyridine, 0.03 M LiTFSI in acetonitrile, and 0.0035 M FK209 Co(III) TFSI salt in acetonitrile. The spiro-OMeTAD layer was deposited by spin-coating at 3000 rpm for 20 s. Finally, 70 nm gold electrodes were thermally evaporated under a vacuum of 10^{-7} torr.

Module fabrication.

Perovskite solar modules consisted of six and eight sub-cells connected in series on 6.5 cm × 7 cm and 5 cm × 5 cm substrates, respectively. FTO substrates were laser-scribed (20 W, 1064 nm, 65 kHz) with a width of 50 μm (P1) to separate the sub-cells. The deposition processes for the ETL, passivation layer, and HTL were the same as the solar cells. The perovskite films were deposited by the vacuum flash-assisted solution process (VASP) in a N_2-filled glovebox. The perovskite precursor (1.3 M) was spin-coated at 1000 rpm for 10 s and 5000 rpm for 20 s, respectively. The substrates were immediately transferred into a vacuum chamber and quickly pumped to a vacuum level of 2-5 Pa. After 20 s, the chamber was released, and the perovskite films were annealed at 100 °C for 50 min and 150 °C for 10 min. Then P2 was laser-scribed (0.4 W, 1030 nm, 200 kHz) with a width of

150 μm. After the gold deposition, 100 μm-width P3 lines were laser-scribed (0.4 W, 1030 nm, 200 kHz) to complete the module fabrication. The geometric fill factor (GFF) was 93% and 91% for the smaller and larger modules, respectively.

Characterizations.

The *J-V* characteristics were measured in air at room temperature using a Keithley 2400 source under simulated AM 1.5 G irradiation (100 mW cm^{-2}) using a Xe arc lamp from a Sciencetech A1 Light Line Class AAA solar simulator (calibrated by a reference solar cell from Sciencetech (SCI-REF-Q) before measurement). No preconditioning of the device was applied before the measurement. The scanning step was 20 mV for solar cells and 50 mV for modules. The scanning rate was 70 mV/s. The active area of the solar cells was defined by an opaque metal mask with a square aperture of area of 0.0625 cm^2. The aperture area of small and large modules was defined by an opaque metal mask with rectangular apertures of 15.28 and 30.86 cm^2, respectively.

Operational stability tests were performed on the unencapsulated solar cells with a nitrogen flow of ~30 mL/min under 1-sun illumination from a white LED. For humidity stability, the unsealed solar cells were kept in the ambient of ~45% relative humidity (RH) monitored by a hygrometer at room temperature in the dark. For thermal stability, the unencapsulated solar cells were heated at 85℃ in nitrogen in the dark. The damp-heat stability test was conducted on the encapsulated modules in a sealed box with ~85% RH and an 85℃ atmosphere. The reverse bias stability with bypass diodes was conducted by applying a constant $-V_{mpp}$ on the perovskite module in the dark.

EQE spectra were taken using an Enlitech QE-R spectrometer. ToF-SIMS measurement was conducted on an IONTOF M6 instrument with a primary Bi source of 30 keV and an analysis area of 50 × 50 μm^2. SEM images were taken by JEOL JSM-7900FLV. The operating voltages for surface and cross-section images were 5 kV and 15 kV, respectively. PL mapping was conducted on a Nano Raman and TERS System integrated with SWIFT and DuoScan technologies. A 473 nm laser was used for excitation. KPFM was performed on Bruker Photocurrent and Thermal AFM with Pt/Ir-coated cantilevers. The scan rate was 0.25 Hz and scan area was 5 × 5 μm^2. Photoluminescence quantum yield of the solid films were collected by a fiber coupled spectrometer (QE-Pro Ocean Optics) in an integrating sphere under the excitation of a power-tunable continuous wave diode laser (405 nm). The power of the excitation light was measured in free space by a power meter (Ophir).

FTIR was performed on a Bruker Tensor 37 FTIR spectrometer. TRPL spectra were collected using an FS5 spectrofluorometer (Edinburgh Instruments) with an excitation wavelength of 373 nm. XPS was performed on the NEXSA G2 instrument with an *X*-ray spot size of 200 μm. XRD patterns were collected using a Rigaku Miniflex diffractometer with Cu Kα_1 radiation. GIWAXS measurement was conducted at the Brockhouse X-ray Diffraction and Scattering Sector Low Energy Wiggler (BXDS-WLE) beamline of the Canadian Light Source (CLS).[28] An energy of 15.12 keV (λ = 0.82 Å) was selected using a Si(111) monochromator. Patterns were collected on a Rayonix MX300 detector operating in 8x8 binning mode placed at a distance of 328.04 mm from the sample. A 4.0 mm circular beamstop with an embedded photodiode was used to block the direct beam and to align the sample height and incident angle (theta). Images were calibrated using LaB6 (NIST SRM 660b) and processed via the Nika software package[29] and the GIXSGUI MATLAB plug-in.[30] TEM was conducted on JEOL ARM200CF. The samples were prepared on Lacey carbon-coated TEM grid. The contact angle was conduced on VCA Optima XE.

DFT calculations

First-principles calculations based on density functional theory (DFT) were carried out using the Vienna Ab initio Simulation Package (VASP).[31] The generalized gradient approximation (GGA) of the Perdew-Burke-Ernzerhof (PBE) functional was employed as the exchange-correlation functional.[32] DFT-D3 method for the van der Waals (vdW) correction was included.[33] The plane-wave cutoff energy was 400 eV. The energy and force convergence criteria were set to 10-5 eV and 0.03 eV·Å−1, respectively. The binding energies (E_b) of ligands with the perovskite surface were calculated as *E*(ligand@perovskite)-*E*(ligand)-*E*(perovskite), where *E*(structure) is the total energy of the corresponding structures. The electrostatic potentials of the ligands were calculated in the Gaussian 09 package at the B3LYP/def2TZVP level with DFT-D3.

Reporting summary

Further information on research design is available in the Nature Portfolio Reporting Summary linked to this article.

Data availability

The data that support the findings of this study are available from the corresponding authors on reasonable request.

Acknowledgements

This work was supported under award number OSR-CRG2020-4350.2. EHS acknowledges support from the Office of Naval Research (ONR) N00014-20-1-2572. M.G.K. was supported by ONR grant N00014-20-1-2725. This work made use of the SPID, EPIC, Keck-II, and NUFAB facilities of Northwestern University's NUANCE Center, which has received support from the SHyNE Resource (NSF ECCS-2025633), the Int. Institute of Nanotechnology, Northwestern University and Northwestern's MRSEC programs (NSF DMR-1720139, NSF DMR-2308691). The authors acknowledge the IMSERC facilities at Northwestern University, which has received support from the SHyNE Resource (NSF ECCS-2025633) and Northwestern University. Part of the research described in this paper was performed at the Canadian Light Source, a national research facility of the University of Saskatchewan, which is supported by the Canada Foundation for Innovation (CFI), the Natural Sciences and Engineering Research Council (NSERC), the National Research Council (NRC), the Canadian Institutes of Health Research (CIHR), the Government of Saskatchewan, and the University of Saskatchewan. ASRB acknowledges support from King Abdullah University of Science and Technology (KAUST) through the Ibn Rushd Postdoctoral Fellowship Award.

Author Contributions

Y.Y., C.L., Y.D., B.D., and J.X. contributed equally to this work. B.C., M.K.N., M.G.K., and E.H.S., supervised the project. Y.Y. conceived the idea. Y.Y. and C.L. designed the experiments and performed the main characterizations. J.X. designed and conducted the DFT calculations. Y.D. and B.D. helped to perform solar cell and module fabrication. J.Y. and X.H conducted the TEM measurement. J.L. helped with the crystallography analysis. S.S.H. and V.K.S. conducted the thermal cycling stability test. L.G. performed the PLQY and GIWAXS measurements and were helpful with the data analysis. A.S.R.B. conducted the contact angle test. A.L., H.Z., and S.M.P were helpful with the construction of the manuscript and revised the manuscript. Y.Y. and C.L. wrote the first draft of the manuscript. All the authors revised and approved the manuscript.

Competing Interests Statement

The authors declare no competing financial interests.

References

1 Ding, Y. *et al.* Single-crystalline TiO_2 nanoparticles for stable and efficient perovskite modules. *Nat. Nanotechnol.* **17**, 598-605 (2022).

2 You, S. *et al.* Radical polymeric p-doping and grain modulation for stable, efficient perovskite solar modules. *Science* **379**, 288-294 (2023).

3 Liu, C. *et al.* Tuning structural isomers of phenylenediammonium to afford efficient and stable perovskite solar cells and modules. *Nat. Commun.* **12**, 6394 (2021).

4 Park, J. *et al.* Controlled growth of perovskite layers with volatile alkylammonium chlorides. *Nature* **616**, 724-730 (2023).

5 Bu, T. *et al.* Lead halide-templated crystallization of methylamine-free perovskite for efficient photovoltaic modules. *Science* **372**, 1327-1332 (2021).

6 Green, M. A. *et al.* Solar cell efficiency tables (Version 60). *Prog. Photovolt.: Res. Appl.* **30**, 687-701 (2022).

7 Yang, M. *et al.* Perovskite ink with wide processing window for scalable high-efficiency solar cells. *Nat. Energy* **2**, 17038 (2017).

8 Ren, A. *et al.* Efficient Perovskite Solar Modules with Minimized Nonradiative Recombination and Local Carrier Transport Losses. *Joule* **4**, 1263-1277 (2020).

9 Jiang, Q. *et al.* Surface passivation of perovskite film for efficient solar cells. *Nat. Photonics* **13**, 460-466 (2019).

10 Yang, Y. *et al.* Bi-functional additive engineering for high-performance perovskite solar cells with reduced trap density. *J. Mater. Chem. A* **7**, 6450-6458 (2019).

11 Zhang, Y. *et al.* A Strategy to Produce High Efficiency, High Stability Perovskite Solar Cells Using Functionalized Ionic Liquid-Dopants. *Adv. Mater.* **29**, 1702157 (2017).

12 Jeong, J. *et al.* Pseudo-halide anion engineering for α-FAPbI3 perovskite solar cells. *Nature* **592**, 381-385 (2021).

13 Min, H. *et al.* Hot-Casting-Assisted Liquid Additive Engineering for Efficient and Stable Perovskite Solar Cells. *Adv. Mater.* **34**, 2205309 (2022).

14 Li, N. *et al.* Cation and anion immobilization through chemical bonding enhancement with fluorides for stable halide perovskite solar cells. *Nat. Energy* **4**, 408-415 (2019).

15 Bai, S. *et al.* Planar perovskite solar cells with long-term stability using ionic liquid additives. *Nature* **571**, 245-250 (2019).

16 Liu, Y., Lorenz, M., Ievlev, A. V. & Ovchinnikova, O. S. Secondary Ion Mass Spectrometry (SIMS) for Chemical Characterization of Metal Halide Perovskites. *Adv. Funct. Mater.* **30**, 2002201 (2020).

17 Kim, D. H., Whitaker, J. B., Li, Z., van Hest, M. F. A. M. & Zhu, K. Outlook and Challenges of Perovskite Solar Cells toward Terawatt-Scale Photovoltaic Module Technology. *Joule* **2**, 1437-1451 (2018).

18 Li, M.-H. *et al.* Highly Efficient 2D/3D Hybrid Perovskite Solar Cells via Low-Pressure Vapor-Assisted Solution Process. *Adv. Mater.* **30**, 1801401 (2018).

19 Mihály, J. *et al.* FTIR and FT-Raman Spectroscopic Study on Polymer Based High Pressure Digestion Vessels. *Croatica Chem. Acta.* **79**, 497-501 (2006).

20 Brakkee, R. & Williams, R. M. Minimizing Defect States in Lead Halide Perovskite Solar Cell Materials. *Appl. Sci.* **10**, 3061 (2020).

21 Wang, R. *et al.* Constructive molecular configurations for surface-defect passivation of perovskite photovoltaics. *Science* **366**, 1509-1513 (2019).

22 Yoo, J. W. *et al.* Efficient perovskite solar mini-modules fabricated via bar-coating using 2-methoxyethanol-based formamidinium lead tri-iodide precursor solution. *Joule* **5**, 2420-2436 (2021).

23 Zhao, Y. *et al.* Inactive $(PbI_2)_2RbCl$ stabilizes perovskite films for efficient solar cells. *Science* **377**, 531-534 (2022).

24 Khenkin, M. V. *et al.* Consensus statement for stability assessment and reporting for perovskite photovoltaics based on ISOS procedures. *Na. Energy* **5**, 35-49 (2020).

25 Zhu, J. *et al.* Formamidine disulfide oxidant as a localised electron scavenger for >20% perovskite solar cell modules. *Energy Environ. Sci.* **14**, 4903-4914 (2021).

26 Wang, C. *et al.* Perovskite Solar Cells in the Shadow: Understanding the Mechanism of Reverse-Bias Behavior toward Suppressed Reverse-Bias Breakdown and Reverse-Bias Induced Degradation. *Adv. Energy Mater.***13**, 2203596 (2023).

27 Bowring, A. R., Bertoluzzi, L., O'Regan, B. C. & McGehee, M. D. Reverse Bias Behavior of Halide Perovskite Solar Cells. *Adv. Energy Mater.* **8**, 1702365 (2018).

28 Leontowich, A. F. G. *et al.* The lower energy diffraction and scattering side-bounce beamline for materials science at the Canadian Light Source. *J. Synchrotron Radiat.* **28**, 961-969 (2021).

29 Ilavsky, J. Nika: software for two-dimensional data reduction. *J. Appl. Crystallogr.* **45**, 324-328 (2012).

30 Jiang, Z. GIXSGUI: a MATLAB toolbox for grazing-incidence X-ray scattering data visualization and reduction, and indexing of buried three-dimensional periodic nanostructured films. *J. Appl. Crystallogr.* **48**, 917-926 (2015).

31 Kresse, G. & Furthmüller, J. Efficient iterative schemes for ab initio total-energy calculations using a plane-wave basis set. *Phys. Rev. B.* **54**, 11169-11186 (1996).

32 Perdew, J. P., Burke, K. & Ernzerhof, M. Generalized Gradient Approximation Made Simple. *Phys. Rev. Lett.* **77**, 3865-3868 (1996).

33 Lee, K., Murray, É. D., Kong, L., Lundqvist, B. I. & Langreth, D. C. Higher-accuracy van der Waals density functional. *Phys. Rev. B.* **82**, 081101 (2010).